WPS1-PR(17) 18033

S Bozhenkov et al.

Thomson scattering diagnostics at Wendelstein 7-X and its performance in the first operation phase

Preprint of Paper to be submitted for publication in
Journal of Instrumentation

This work has been carried out within the framework of the EUROfusion Consortium and has received funding from the Euratom research and training programme 2014-2018 under grant agreement No 633053. The views and opinions expressed herein do not necessarily reflect those of the European Commission.

Thomson scattering diagnostics at Wendelstein 7-X and its performance in the first operation phase.

S.A. Bozhenkov[1], M. Beurskens[1], A. dal Molin[2], G. Fuchert[1], M. Hirsch[1], U. Höfel[1], J. Knauer[1], E. Pasch[1], M.R. Stoneking[3], J. Svensson[1], H. Trimino Mora[1], R.C. Wolf[1] and W7-X team

[1] Max-Planck-Institut für Plasmaphysik, D-17491 Greifswald, Germany

[2] Università degli Studi di Milano-Bicocca, Milan, Italy

[3] Lawrence University, Appleton, Wisconsin, USA

E-mail: `sergey.bozhenkov@ipp.mpg.de`

Abstract. Optimized stellarator Wendelstein 7-X started operation in December 2015 and will perform the first divertor experiments in the second half of 2017. The W7-X Thomson scattering system is an essential diagnostic for electron density and temperature profiles. In this paper the Thomson scattering diagnostic is described in details, including setup, calibration procedures, data evaluation, experimental results and their comparison with other diagnostics, and development plans.

The W7-X system is a Nd:YAG setup with up to five lasers, two sets of lenses covering the whole plasma cross-section, fiber bundles and filter based polychromators. To save hardware costs, two scattering volumes are measured with a single polychromator, with one of the fiber bundles having a delay loop of 20 m. The relative spectral calibration is carried out with the help of a broadband supercontinuum light source. The absolute calibration is performed by observing Raman scattering in nitrogen. The electron temperatures and densities are recovered by Bayesian modelling. Details of the modelling including a discussion of possible posterior distributions are given. In the first campaign, the Thomson scattering diagnostic provided temperature profiles comparable with an independently calibrated electron cyclotron emission diagnostic and densities in agreement with the single channel dispersion interferometer within about 10%.

1. Introduction

Wendelstein 7-X is a large optimized stellarator with superconducting coils [1, 2]. The optimization includes low neoclassical transport, high equilibrium β, good MHD properties, small bootstrap current and good fast-ion confinement. The aim is to demonstrate the viability of the stellarator line as a fusion reactor [3]. The optimization procedure is detailed in [4] and a historical perspective is presented in [5].

W7-X operation started with a limiter campaign, named OP1.1, that lasted from December 2015 until March 2016. Five graphite inboard limiters defined the plasma edge [6] and only ECRH discharges with total injected energy below 4 MJ were administratively allowed. The campaign was devoted to an integrated commissioning of the machine, but some promising physics results were achieved as well. Plasmas with electron temperatures of up to 7 keV, ion temperatures of up to 2 keV and electron densities of up to $3 \cdot 10^{19}$ m^{-3} were realized [7, 8].

To achieve steady-state operation with ECRH heating of up to 10 MW, W7-X will be equipped with island divertor [9, 10]. First in campaign OP1.2 planned for the second half of 2017, the test graphite divertor with inertial cooling will be used to establish the divertor operation and to explore the operational space. Later in campaign OP2, the water-cooled graphite divertor of the same shape as the test one will be installed with the aim of realizing up to 30 minutes discharges [11]. The different W7-X campaigns and the corresponding machine capabilities are detailed in [3].

A good diagnostic coverage is essential for physics studies at W7-X. In particular, profile information for electron temperature and density is necessary e.g. for confinement and transport studies [12,13], for investigations of profile resilience with ECRH deposition [8] etc., and is also an important input for many numerical codes. At W7-X a Thomson scattering system is a standard profile diagnostic for electron temperature and density. In this paper the W7-X Thomson scattering is described in details, and a summary of the system performance in the first campaign OP1.1 as well as plans for the future development are presented.

Thomson scattering is a process of scattering of an electromagnetic wave by free charged particles. If applied to the plasma conditions, a free electron is accelerated by the wave fields; and as a result, it emits scattered wave at the Doppler shifted frequency. In the case the scattering wave vector $\boldsymbol{k} \equiv \boldsymbol{k}_s - \boldsymbol{k}_i$ is large enough for its product with the Debye length λ_D to meet the condition $k\lambda_D >> 1$, the scattering from electrons sums incoherently. The intensity of the scattered wave is then proportional to the electron density and its spectrum reflects the electron velocity distribution, i.e. the electron temperature. Incoherent Thomson scattering is a well established experimental technique [14], which is successfully applied at many fusion machines [15–17]. To overcome the disturbing plasma radiation powerful lasers are applied. Nd:YAG lasers are often chosen because of their commercial availability and a lower plasma light contamination in the near-infrared region.

The spectrum of the incoherent scattering can be calculated by taking an integral over

the electron distribution [14]. For fusion relevant conditions a full relativistic treatment is required. An analytical expression for the scattered power P_s was obtained for both the incident and the observed light polarized perpendicular to the scattering plane [18, 19]:

$$\frac{d^3P_s}{d\epsilon d\Omega d^3r} = r_e^2 n_e \langle S_\ell \rangle S(\epsilon, \theta, \alpha), \tag{1}$$

where r_e is the classical electron radius, S_ℓ is Poynting vector of the incident laser light, θ is scattering angle, $\epsilon \equiv (\lambda - \lambda_\ell)/\lambda_\ell$ is normalized wavelength shift and α is normalized inverse temperature $m_e c^2/(2T_e)$. The expression for the spectral density function $S(\epsilon, \theta, \alpha)$ is lengthy but can be found in the cited paper.

Because of signal to noise considerations, the scattered spectrum is usually measured only in a few spectral intervals, e.g. five for the W7-X setup. Such a polychromator system is realized by a set of interference filters and photodiodes. The signal registered by a polychromator channel i can be approximated as:

$$\left(\int s dt\right)_i = n_e E_\ell \frac{r_e^2}{hc} \cdot \delta\Omega g_0 \cdot \int\int S(\epsilon, \theta, \alpha) \cdot \frac{\lambda}{\lambda_\ell} \cdot \frac{g_i(\lambda)}{g_0} \cdot dL d\lambda, \tag{2}$$

where the time integration is over the laser pulse, E_ℓ is the laser pulse energy, $\delta\Omega$ is the system solid angle, $g_i(\lambda)$ is the absolute sensitivity including the filter transmission and electronic gains, $g_0 \equiv g_r(\lambda_r)$ is the absolute sensitivity of a reference channel at a reference wavelength. The integration on the right hand side is over the wavelengths and over the length of the observation volume along the laser line. If the plasma parameters do not change significantly in the observation volume the latter integration reduces to multiplication by the volume length δL.

Practical applications of Thomson scattering require a careful system calibration. Since it is often not possible to absolutely calibrate all spectral channels, instead the calibration is split into two parts. According to equation 2, the wavelength integration can be performed with the relative channel sensitivities $g(\lambda)/g_0$, where the reference value can be chosen rather arbitrarily. The determination of this relative values is called spectral calibration. The absolute sensitivity of the system is given by the factor $\delta\Omega\delta L g_0$ and is a subject to the absolute system calibration. The latter can be done by using Rayleigh or Ramman scattering. The quality of the calibration defines a systematic uncertainty of the plasma measurements.

The W7-X incoherent Thomson scattering system is a Nd:YAG setup using polychromators for spectral analysis. The laser light is guided through the plasma roughly horizontally and passes close to the magnetic axis, e.g. for a direct measurement of the Shafranov shift. Two sets of lenses observe the whole plasma cross-section: one set for the inboard and the outboard halves of the profile. The optical setup is decoupled from the machine to guarantee optical stability. The scattered light is collected into fiber bundles relaying it to filter based polychromators. The light is detected with avalanche photodiodes, and after shaping and ADC sampling the signals are stored for further processing. A peculiarity of the setup is that fiber bundles from different scattering volumes are fused into a single polychromator, thus reducing the hardware costs.

Calibration procedures and data processing are essential parts of the system. The

relative spectral calibration is carried out with the help of a pulsed supercontinuum light source and of a scanning monochromator. The front optics, the fibers, the interference filters,the avalanche photodiodes and the electronics are covered by this calibration. The transmission of the vacuum windows is added separately. The second step is the absolute calibration with Raman scattering in nitrogen. The Raman scattering signal is observed in two spectral channels. The results from these channels are generally consistent, with the remaining differences being attributed to the unidealness of the spectral calibration. The uncertainty of the absolute calibration is directly related to the systematic uncertainty of the electron density.

The temperatures and densities are recovered by Bayesian modelling with Minerva framework [20]. Minerva is a Java framework convenient for practical applications, adopted also for other diagnostics at W7-X. As compared to the usual ratio method the Bayesian approach provides asymmetries of the uncertainties due to deviation from Gaussian distribution, and the cross-correlation between measured density and temperature [21, 22]. It is straightforward to include uncertainties on the calibration parameters, to introduce a profile description [23], or to combine multiple diagnostics, e.g. for a self-consistent equilibrium reconstruction. In this work, the Thomson Bayesian model is developed and is used to analyze performance of the W7-X system. Examples of different types of the posterior distribution are presented and the cases with pronounced asymmetric uncertainties and cross-correlation are indicated. Scalings of the uncertainties of the plasma parameters with temperature and with signal to noise ratio are presented. For high signal to noise conditions, the W7-X setup with five spectral channels is found to recover the temperature and density without cross-correlation between about 10 eV and 10 keV.

The W7-X Thomson scattering system was operational from the very first day of campaign OP1.1 with 10 scattering volumes at the outboard half of the profile. The system proves to perform reliably and to provide vital data [7, 8, 12, 13]. A general consistency of the temperature profiles between the Thomson scattering and the W7-X ECE diagnostic, and of Thomson scattering density profiles with the line integrated interferometry is found. The remaining differences will be addressed in future experiments. For the next campaign OP1.2, the Thomson system will be upgraded: at the outboard side six more volumes will be added; the inboard side will be covered with in 79 volumes; three lasers will be operational. The spatial resolution of the inboard half will vary between about 15 mm in the core to about 6 mm in the outer part where sharp gradients can be expected. The standard time resolution will be increased to 30 Hz, in addition a burst mode with short pulse trains of up to 10 kHz is foreseen.

The rest of the paper is organized in the following way: first in section 2 the hardware setup of the W7-X Thomson scattering is described; then in sections 3 and 4 details of the spectral and absolute calibrations are covered; in section 5 the data processing and Minerva modelling are explained, and numerical studies of the system capabilities are presented; in section 6 experimental results from the first W7-X campaign are shown; and finally in section 7 the results of the paper are summarized.

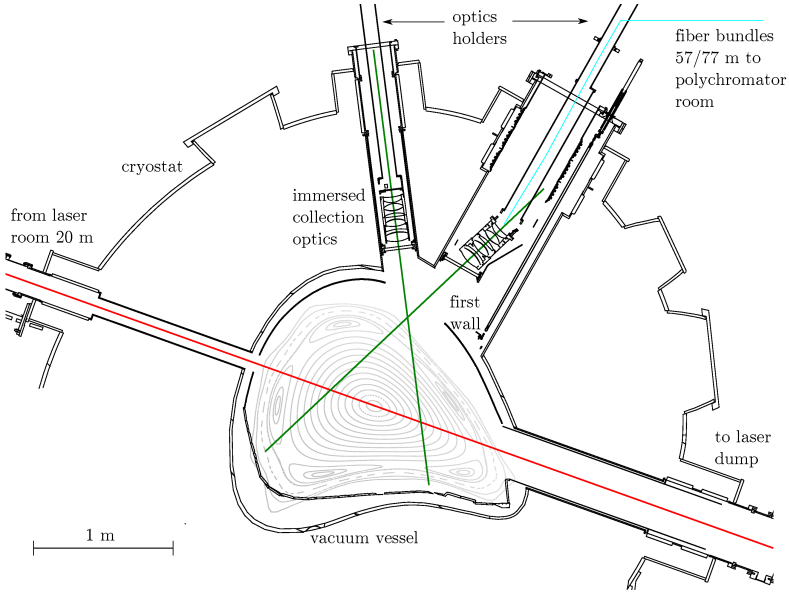

Figure 1. W7-X Thomson scattering setup. The laser light enters the vessel from the inboard side of the machine, passes through the plasma center, and leaves the vessel at the outboard side. The full plasma cross-section is observed with two sets of optics. The scattered light is transferred with fiber bundles to a polychromator room.

2. W7-X Thomson scattering system

The W7-X Thomson scattering diagnostic is a Nd:YAG system. An overview of the setup is shown schematically in figure 1. The laser light, $\lambda = 1064$ nm, is guided through the plasma center and is dumped outside of the vacuum vessel. The light scattered by plasma is collected with front optics into a set of fiber bundles, each fiber bundle defining a scattering volume. The fiber bundles transfer the light to polychromators, where the spectral analysis and the light detection is performed. The signals are digitized, stored into the experimental Archive, and are used to reconstruct both the electron temperature and the electron density. In this section, a brief overview of the setup is given, for further details paper [24] is recommended.

The system is designed for operation with up to five Nd:YAG lasers, which can be triggered either simultaneously to increase the pulse energy or with a delay to increase the time resolution. For an easy access and maintenance, the lasers are located in a dedicated laser room. The laser light is delivered to the plasma vessel with a carefully designed and about 20 m long system of dielectric mirrors. The lasers, pulse energy from 0.7 to 2.4 J, pulse length about 10 ns, repetition rate 10 Hz, are linearly polarized and the polarization is delivered perpendicular to the scattering plane. In the first campaign OP1.1, only one laser was operated, i.e. the time resolution was limited to 100 ms. In the next campaign OP1.2, three lasers will be available resulting in increased sampling frequency of 30 Hz.

After leaving the vessel, the laser light is directed to the laser energy monitor and to the beam dump both at the distance of about 3 m away from the output port. The input

and output vacuum windows are located at the ends of the port tubes. This together with the long distance to the dump minimizes the disturbance of the measurements by the stray radiation. The spectral filters in the polychromators provide an additional suppression of the laser light.

The full plasma cross-section of about 1.6 m is observed with two sets of optics specially designed for the wavelength range from 700 to 1064 nm [25]. Each optics set observes one half of the cross-section, and therefore they can be referred to as inboard and outboard. The main parameters of the optics are: focal length is 172 mm; distance to the laser line is about 1.3 m; diameter of the outboard optics 160 mm; the size of the inboard optics is 90×160 mm; typical solid angle is about 8 msr; both systems are designed for fibers with numerical aperture of up to 0.37; the optical demagnification varies between 7 and 11. The optics sets are mounted on retractable manipulators and during measurements are placed inside the ports at the air side of the vacuum windows. The optics are retracted to readjust or replace fiber bundles, and for protection during baking out of the machine.

The laser mirrors and the optics sets are mounted on a special structure called Thomson bridge [24]. The Thomson bridge is mechanically decoupled from the vacuum vessel and from the magnetic system, thus guaranteeing optical stability. Indeed, the experiments in OP1.1 showed that the system remains adjusted and performs well during an experimental day. Losses of the adjustment happened between experimental days, when a general access to the bridge was open. The system operation was guarantied by an inspection and a fine adjustment before experiments. An automated adjustment with monitoring cameras and remotely-steerable mirrors is under development.

The scattered light is collected into fiber bundles transferring it to polychromators for spectral analysis. Arrangement of the fibers in the imaging plane defines the number of the observed scattering volumes and the spatial resolution, as illustrated in figure 2. In the first campaign, only the outboard part of the system was operated with 10 fiber bundles of rectangular cross-section 3.2×1.1 mm^2, left part of the figure. One of the channels was initially placed into the scrape-off layer and showed a reliable signal, but was relocated to the core region for a better core coverage and a better comparison between channels.

Two types of fibers were tested: eight of the bundles are with quartz core and have numerical aperture of 0.29; two bundles are with Ge-doped core and have numerical aperture of 0.37. It is found, however, that because of a more sparse packing of the fibers in the bundle the Ge-doped bundles do not show advantage in terms of the signal quality. Therefore, the quartz fiber with numerical aperture of 0.29 will be used for the rest of the system.

The profile coverage will be improved for the next experimental campaign OP1.2, as shown in the right part of figure 2. The outboard side will be extended with six additional fiber bundles of the same size as the first 10 ones. This extension is possible without modifying any mechanical components by filling available slots in the fiber holder. It can be expected that the 16 channel outboard side can be operated reliably.

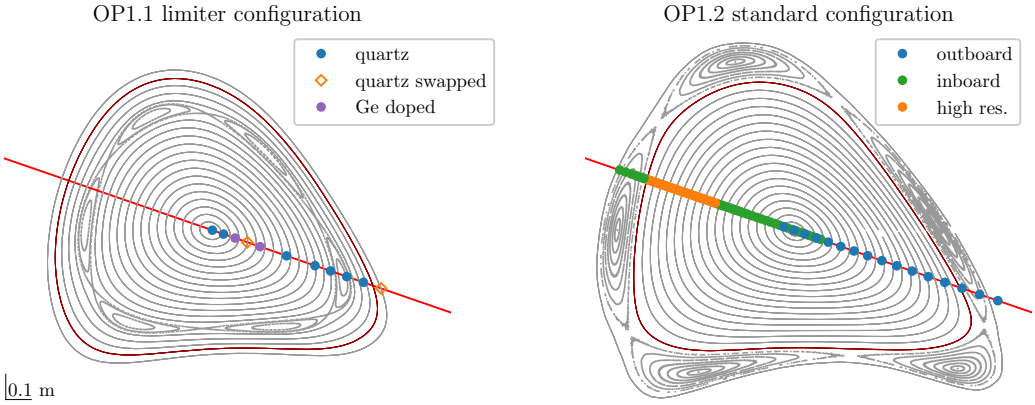

Figure 2. Scattering volumes in the OP1.1 campaign limiter configuration (left) and standard divertor configuration of OP1.2 campaign (right). In OP1.1 the outboard side was covered with 10 volumes, two of the volumes were observed with Ge-doped fibers. One of the fibers was moved in the middle of the campaign from the edge to the core. In the next campaign, OP1.2, the outboard side will be extended to 16 volumes, and the inboard side will be covered with 79 volumes. In both cases the last closed flux surface (LCFS) is indicated.

The inboard part of the profile will be taken into operation with 79 volumes. Here fiber bundles of different lengths without ferrule will be densely packed side by side. In the outer part of plasma, where large gradient can be expected, the inboard system shows spatial resolution of about 6 mm in effective radius, highlighted with colour in figure 2. In the center the inboard and outboard parts overlap with about 10 cm, which can be used as a self-consistency check.

The spatial resolution of the system is defined as the distance between the centers of the two nearby scattering volumes. This value measured in effective radius is presented in figure 3 for both parts of the system. The resolution of the outboard side changes from about 3 cm in the center to about 5 cm at the edge. For the inboard side, the areas with different resolution are defined by the used length of the fiber bundles: in the core the resolution is 15 mm or 8 mm; in the high resolution area it is 6 mm; in the island region the resolution is about 11 mm. The shown values are calculated for the standard W7-X divertor configuration, but the changes with magnetic configuration are small.

The high resolution inboard part of the system can be expected to be sensitive to the experimental conditions. Higher laser energies and densities can be necessary for reliable measurements. The signal to noise ratio can be improved by filtering out impurity lines and using a polariser to diminish Bremsstrahlung contamination. These options are presently under investigation.

Positions of the scattering volumes are accurately measured during maintenance periods with a laser tracking system. The measured positions can be mapped to plasma coordinates by using e.g. plasma equilibrium code VMEC, possibly self-consistently.

The fiber bundles transfer the scattered light to polychromators for spectral analysis.

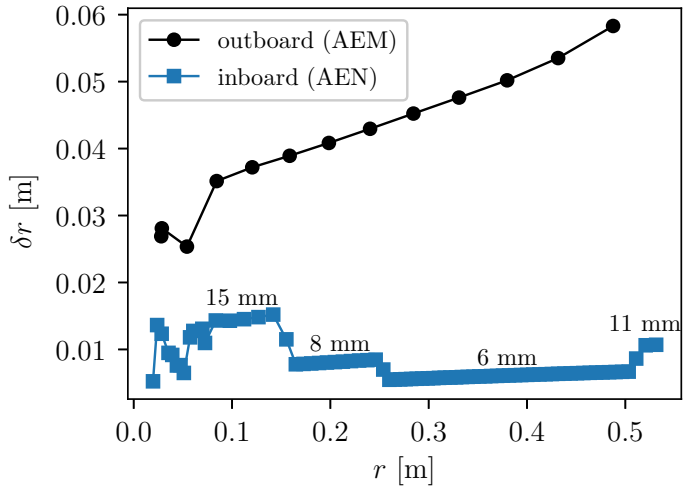

Figure 3. Resolution of the Thomson scattering system for the standard divertor configuration of campaing OP1.2. The resolution is defined as the distance between the centers of two neigbouring volumes. The distance is measured as effective radius, where the LCFS radius is about 0.5 m. The inboard and outboard sides are shown separately. The inboard side consists of regions with different resolution.

To save hardware costs, some bundles are combined to a single polychromator, with one of the bundles having a delay loop of 20 m to separate the signals in time. In campaign OP1.1 all fibers were paired, with one end of 57 m and the second one of 77 mm. Such an approach proved to be reliable and to cause a tolerable increase in the noise level. An example of the delayed signals can be found later in figure 5. The fiber bundles for the inboard side will be also combined: in areas with high resolution two volumes per polychromator and in the core with resolution of 15 mm three volumes per polychromator.

The spectral analysis of the scattered light is performed with filter based polychromators. The optical design of polychromators is for numerical aperture of 0.37 and fiber bundle of 3 mm in diameter. Five spectral channels are used to cover the electron temperatures from about 10 eV up to about 10 keV: 750–920 nm, 920–1000 nm, 1000–1035 nm, 1035–1051 nm and 1051–1061 nm. For even higher temperatures six channel polychromators will be introduced in campaign OP1.2, as discussed later in the paper, see e.g. figure 9. The optical signals are registered with temperature stabilized avalanche photodiodes.

The photodiode outputs are AC filtered to remove the constant background, amplified and digitized with sampling rate of 1 GS/s and 14 bit vertical resolution. The acquisition system records time resolved laser pulses, which helps to recognize reflection events and improves the signal to noise ratio. The digitized signals are used in the post-analysis to recover both the most likely temperature and density.

It is to be noted that presently the system is operated without a polariser, which is required for a strict application of Naito formula, equation 1. Numerical integration of

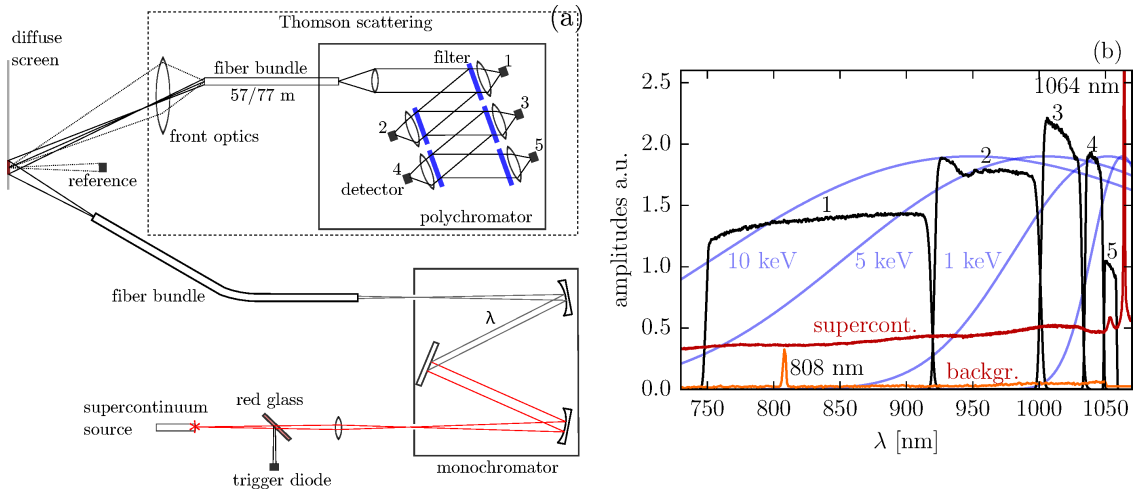

Figure 4. Spectral calibration. (a) - spectral calibration setup. A narrow wavelength range is selected from the output of a supercontinuum source with a monochromator. The single wavelength is used to illuminate a diffuse screen in front of the optics. (b) - typical calibration results. In the figure also Thomson scattering spectra for temperatures of 0.1, 1, 5 and 10 keV and supercontinuum spectrum are given.

the full expression demonstrates that the correction is negligible for the present experimental conditions.

3. Spectral calibration

The relative spectral calibration provides factors $g(\lambda)/g_0$ for all spectral channels of all scattering volumes, see equation 2. The calibration procedure at W7-X includes the front optics, the fiber bundles, the polychromators and the electronics. The vacuum windows are measured separately and are taken into account additionally. Possible vignetting by the in-vessel structures is presently not accounted for.

A sketch of the spectral calibration setup is shown in figure 4a. A supercontinuum light source (Super-K compact by NKT Photonics) generates about 2 ns long pulses covering a wide spectrum with repetition rate of 30 kHz. A monochromator (Spex 750M) is used to select a narrow wavelength interval for a measurement. The monochromator output is delivered with a fiber bundle to the stellarator hall. During spectral calibration the front optics with the mounted fibers is retracted from the port and a spectrally neutral diffuse screen is placed in front of it. This screen is illuminated with the fiber bundle from the monochromator. In a calibration run the monochromator wavelength is scanned in the range of interest, the intensity reflected by the diffuse screen is monitored with a reference photodiode.

In the calibration setup the angular distribution of the intensity is not necessarily equivalent to that during plasma measurements. In both cases the light collection is limited by the numerical aperture of the fibers. But in the calibration case the light source, i.e.

the screen, is placed much closer to the optical system, which implies that to reproduce the plasma case also a spatial uniformity of the spot is required. This is approximated by illuminating an oversized area. A possible systematic influence of this approach will be investigated in future.

A typical measurement for five spectral channels is illustrated in figure 4b. Each curve was measured with a wavelength step of 0.1 nm and for each wavelength 200 pulses were accumulated for statistics. The change of the amplitudes between channels 4 and 5 is mainly due to the setting of the avalanche voltage of APDs. The supercontinuum spectrum registered with the reference diode can also be found in the figure. The source spectrum is rather flat in the region covered by filters, outside of this region the original Nd:YAG wavelength of 1064 nm is pronounced. This line can be used to estimate the spectral resolution of the measurement and together with an additional line at 808 nm to calibrate the wavelength scale. The spectral resolution is estimated as FWHM of the Nd:YAG line and constitutes about 0.4 nm. For the wavelength calibration the second line is the CW line of the pump diode at 808 nm.

4. Absolute calibration

The absolute calibration of the W7-X Thomson scattering system is performed by using anti-Stokes rotational Raman scattering in nitrogen, as first proposed in [26] and is now used at several fusion experiments [27,28]. The anti-Stokes part of the rotational Raman spectrum consists of multiple narrow lines due to transitions $J \rightarrow J-2$, where J is the rotational quantum number. The integral signal registered by a spectral channel for a

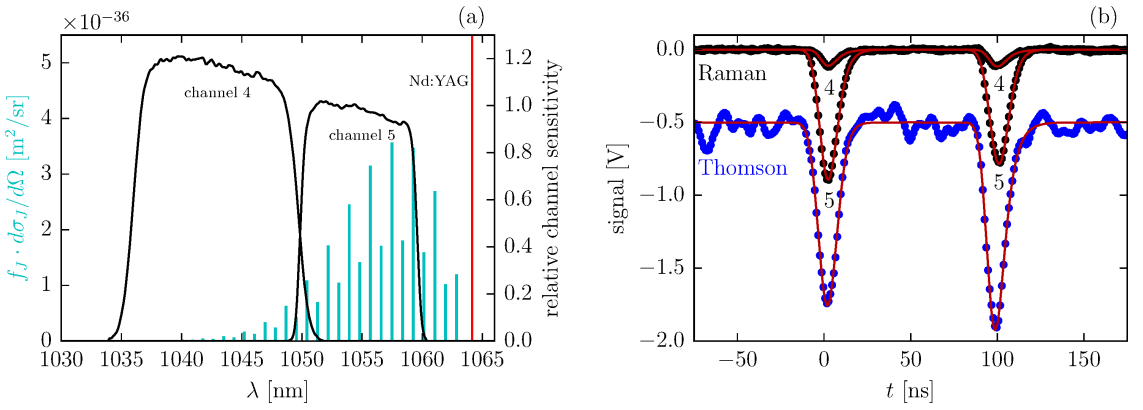

Figure 5. Raman scattering calibration. (a) - anti-Stokes rotational Raman lines in nitrogen. Effective cross sections of the lines including the relative level populations are overlaid with typical spectral curves of two Thomson channels. (b) - typical Raman scattered signals for the spectral channels 4 and 5 at nitrogen pressure of about 100 mbar and laser pulse energy of 1 J. For comparison a Thomson scattering signal from the spectral channel 1 from plasma with T_e of about 6 keV and n_e of about $1.3 \cdot 10^{19}$ m^{-3} and laser pulse energy of 1.5 J is shown with an offset of -0.5 V.

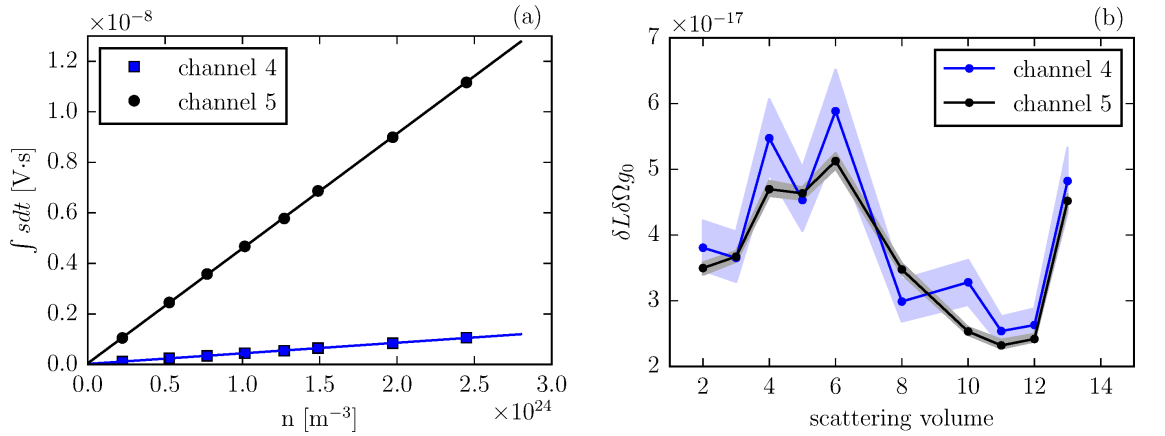

Figure 6. Results of the Raman scattering calibration. (a)- measured signals for spectral channels 4 and 5 in dependence on the nitrogen density. The solid lines are linear fits to the experimental data: $k_4 \approx 4.20 \pm 0.04 \times 10^{-34}$, $k_5 \approx 4.55 \pm 0.02 \times 10^{-33}$. Each data point is averaged over 500 laser pulses. (b) - calibration factor $\delta L \delta\Omega g_0$ for the ten scattering volumes as found from the Raman calibration. The colored areas show the sensitivity to a wavelength shift of ±0.25 nm for the spectral calibration.

laser pulse is found by summing all the lines, compare to equation 2:

$$\left(\int sdt\right)_i = n_{N2} E_0 \cdot \sum_J \frac{d\sigma_J}{d\Omega} f_J \frac{\lambda_J}{hc} \frac{g_J}{g_0} \cdot \delta L \delta\Omega g_0 \equiv n_{N2} E_0 R \cdot \delta L \delta\Omega g_0 \tag{3}$$

Here n_{N2} is the nitrogen particle density, E_0 is the laser pulse energy, $\frac{d\sigma_J}{d\Omega}$ is differential cross-section for the line λ_J, f_J is the fractional population of the upper state and $g_J/g_0 \equiv g_i(\lambda_J)/g_0$ is the relative sensitivity of the system at the wavelength. The product of the scattering volume length δL, solid angle $\delta\Omega$ and the channel sensitivity g_0 including the transmission losses and the reference photodiode gain can be found from linear scaling with gas pressure, provided the relative spectral calibration and the molecular constants. The differential cross-section is [29, 30]:

$$\frac{d\sigma_J}{d\Omega} = \frac{64\pi^4}{45} \frac{3J(J-1)}{2(2J+1)(2J-1)} \frac{\gamma^2}{\lambda_J^4} \cdot F, \tag{4}$$

where F is a factor depending on the scattering geometry and observed polarization. For the case without a polarizer considered here the value of F is 7/4. The value of the anisotropy of the polarizability tensor γ^2 has a weak dependence on the wavelength and was measured to be $(5.1 \pm 0.25) \times 10^{61}$ m^6 for the Nd:YAG wavelength [27]. The relative level population is given by the Boltzmann distribution:

$$f_J = \frac{w_J(2J+1)}{Z} \exp\left(-E_J/kT\right), \tag{5}$$

w_J is a statistical weight, which for nitrogen is 3 for odd values of J and is 6 for even values. The normalization constant Z is chose such that $\sum_J f_J = 1$. The rotational level energy is $E_J = hc(B_0 J(J+1) - D_0 J^2(J+1)^2)$, with molecular constants $B_0 = 1.99 \cdot 10^2$ m^{-1} and $D_0 = 5.76 \cdot 10^4$ m^{-1} taken from [31]. During the measurements at W7-X the temperature of the plasma vessel is monitored with thermocouples, the

gas is assumed to be in thermal equilibrium with the walls.
Anti-Stokes rotational lines of nitrogen are illustrated in figure 5a, where the effective cross-sections including the relative level populations for the room temperature are plotted. The lines have a significant amplitude in the range of the Thomson spectral channels 4 and 5. An example of the measured signals in spectral channels 4 and 5 for nitrogen pressure of about 100 mbar and laser energy of 1 J is given in figure 5b. As expected, the amplitude of the signal in channel 5 is about an order of magnitude higher than in channel 5. The two peaks separated by about 100 ns appear because of combining fiber bundles from two volumes with a delay loop of 20 m. For comparison an example of the Thomson scattered light from the plasma at the density of $1.3 \cdot 10^{19}$ m^{-3} and laser pulse energy of 1.5 J is also shown in the figure. The Thomson scattered signal is offset by -0.5 V for clarity. The Raman signals have a higher signal to noise ratio as compared to the Thomson scattered signal, because in the plasma case a considerable Bremsstrahlung backround noise is present.
Dependence of the Raman signals in the spectral channels 4 and 5 on the nitrogen density is given in figure 6b. Each data point in the plot is averaged over 500 laser pulses; as a consequence, the statistical errors are small. The solid lines in the figure represent the corresponding linear fits. For all the scattering volumes the stray laser light is insignificant, because the fit lines come closely through zero. The slope of the lines can be determined with a statistical error of about 1%.
The calibration factors $\delta L \delta \Omega g_0$ calculated from equation 3 for the scattering volumes used in OP1.1 are plotted in figure 6b and have a small statistical uncertainty. The shape of the dependence of the calibration factor on the channel is dominated by the absolute gain settings of the avalanche photodiodes. The factors calculated using the two spectral channels are of the same order, but do show a noticeable difference for some volumes. This is likely to be related to the details of the spectral calibration, because in the spectral channel 4 the Raman lines are located in the steep region. For example, a small shift of the wavelength scale by 0.25 nm strongly influences the results in channel 4 but not so much in channel 5, and can bring both channels to agreement. However, a uniform shift is not likely the real reason, since it would shift the whole dependence, but it is rather an insufficiently uniform illumination of the light cone during the spectral calibration. The shift of 0.25 nm corresponds to about 2° change in the incidence angle. For channel 5 the corresponding change is about 4%.
The absolute calibration factor $\delta L \delta \Omega g_0$ can be reliably determined from the spectral channel 5 with the individual point error estimated about 4% as caused by an unideal spectral calibration. All values have the same systematic uncertainty of 5% due to the value of the anisotropy of polarizability tensor γ in equation 4. The influence of the temperature on the result is 1 %/K for channel 4 and 0.1%/K for channel 5; and is, therefore, negligible.

5. Data processing

For each laser pulse the acquisition system records time resolved traces of the scattered radiation for all spectral channels. An example of a time trace is given in figure 5b. To reconstruct electron temperatures and densities from such time traces a two stage approach is used. First, the time traces are individually fitted with a model pulse and the time integral of the pulse is found. After the fitting, the found values for all spectral channels of a volume are modelled with Bayesian framework Minerva to simultaneously determine the most likely temperature and density, and their uncertainties.
For the W7-X system, an accurate fitting of the scattered pulse can be performed with a convolution of a Gaussian laser pulse and of the first order low-pass filter. The typical laser pulse full-width-at-half-maximum and the low pass filter time constant are about 10 ns and 3 ns correspondingly. An example of the fitting is shown with solid lines in figure 5b. It is important to mention that the fitting also provides the associated uncertainties, which is essential for Bayesian analysis. The background plasma radiation, which is mainly Bremsstrahlung in OP1.1, contributes considerably to the uncertainty.
Bayesian probability theory contributes a universal approach for determining system parameters from observations. The probability density function of the parameters given the measurements, known as posterior, is expressed as [32]:

$$p(P|D) = \frac{p(D|P) \cdot p(P)}{p(D)} \tag{6}$$

The likelihood of the data given parameters $p(D|P)$ represents the observations, e.g. it can be a Gaussian distribution with a forward model prediction and experimental uncertainties. The prior parameter distribution $p(P)$ incorporates any previous knowledge of the problem and often can be assumed uniform. The evidence $p(D)$ does not influence finding the parameters but is rather a normalization factor, which however turns important for hypothesis testing.
The Bayesian approach for Thomson scattering was previously demonstrated to perform well as compared to the usual ratio method [21] and to provide additional information about asymmetries of the posterior [22]. For W7-X, an independent implementation in Minerva framework is developed.

Minerva [20] is a Java framework for practical applications of Bayesian analysis. It is based on graphical models, i.e. all models are graphs. Each parameter or measurement is reflected by a node of the graph and the edges between the nodes represent deterministic or probabilistic dependencies. Minerva keeps track of the dependencies, which helps to optimize the simulations. The framework allows finding of the maximum of the posterior, sampling of the posterior with Markov-Chain-Monte-Carlo (MCMC) method, and contains implementations of many other useful algorithms.
The graphical model of the Thomson scattering is shown in figure 7. In this example only the electron temperature and the density are considered unknown. Their prior distributions are assumed to be flat between zero and a maximal value plausible for a discharge. The priors are shown as light blue ellipses in the figure. For the present work,

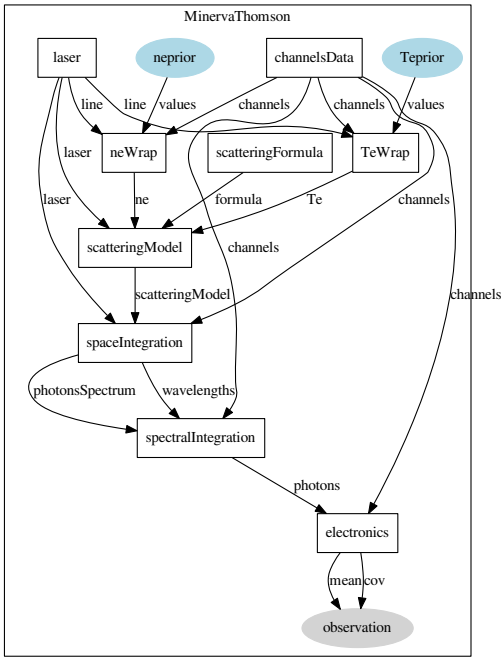

Figure 7. Minerva graph of the Thomson scattering model. Each parameter or measurement is represented by a node. The edges represent deterministic or probabilistic dependendcies. Prior distributions for T_e and n_e are shown as light blue ellipses. The observation node, gray elipse, is a probabilistic node for the comparison of the forward model with the measurements.

each scattering volume is treated independently, but with a small modification a profile description can be connected [23]. The forward model, the part between the priors and the observation node, is a deterministic relation between parameters and the values to be measured. This involves both space and spectral integration and scaling by the electronics. The space integration is considered explicitly to allow treatment of profiles with gradient lengths comparable with the scattering volume length, e.g. in a pedestal region. The forward model is connected to a probability observation node, shown in gray, where it is to be compared with the measurements. The forward model and the observation node together correspond to the likelihood distribution of equation 6, whereas the whole graph is a posterior equivalent.
It is straightforward to elaborate the Thomson model e.g. by adding uncertainties on the calibration parameters or by combining it with other diagnostics. It is to be noted that the forward model itself is not modified, but only additional priors have to be connected to the parameters in question or additional graphs for other diagnostics are to be added. Such more elaborated models will be studied in a future work.

To test the model and to verify performance of the W7-X Thomson system forward-inverse simulations are performed. Some values of temperature T_e and density n_e are used to first forward calculate the signals in all spectral channels and to generate

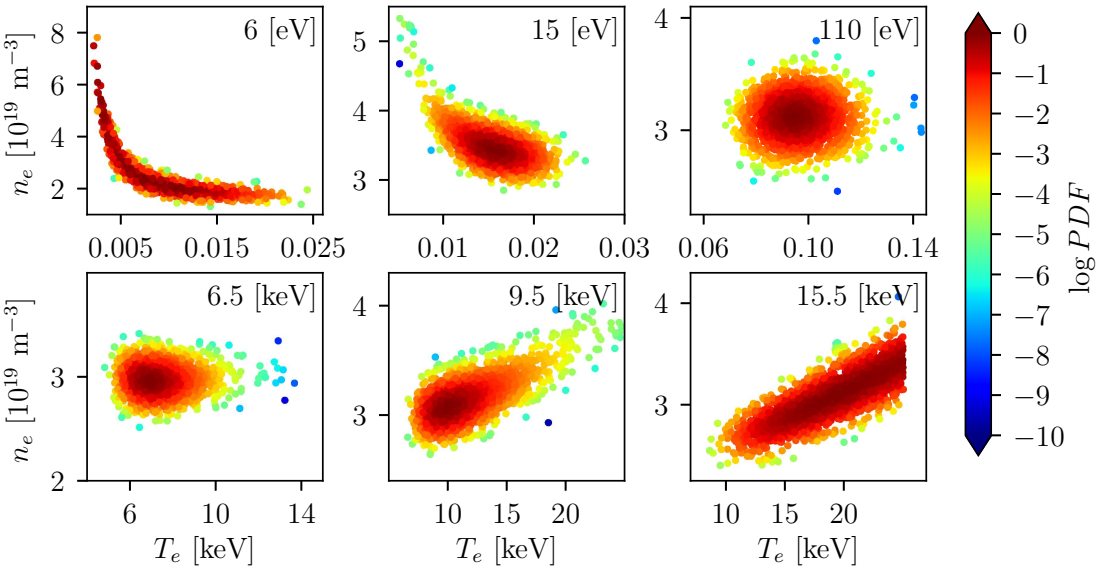

Figure 8. Posterior distributions in the temperature and density plane for different temperatures and density of $3 \cdot 10^{19}$ m^{-3}. The noise level correspond to SNR of about 16. At the edges, for 6 eV and 15.5 keV, there is a dominant cross-correlation between density and temperature. Close to the edges, for 15 eV and 9.5 keV, the cross-correlation has to be considered in estimating the uncertainties. In the mid-temperature range illustrated with 110 eV, the posterior is close to Gaussian with very little or no cross-correlation. Asymmetric error bars can be important even without cross-correlation, shown with 6.5 keV.

synthetic measurements by adding a noise pattern. The generated values are then used as observations and the Minerva model is applied to find the temperature, the density and their uncertainties. Gaussian distribution with a fixed value of the standard deviation σ is employed to describe the noise, the value of σ is a free parameter. A fixed value of σ is closer to real experiment conditions than a fixed signal to noise ratio (SNR) for every spectral channel. The parameters of the model correspond to the W7-X system, including the calibration factors.

Result of a Bayesian model is fully described by the posterior distribution. From the practical point of view, the posterior distribution around the maximum is usually of interest. The latter can be sampled with the MCMC procedure, once the maximum of the distribution is found with an inversion technique. Because the Thomson model analyzed here depends only on two parameters, it is straightforward to illustrate such posteriors. Sampled posterior distributions are presented in figure 8 for several values of the electron temperature. Each point is an MCMC sample, and the colour of the point reflects its probability value with respect to the maximum. For example, points coloured green have the probability about e^{-4}–e^{-5} times less than in the maximum, which corresponds to the 3σ boundary of the normal distribution.

The Thomson posterior is found to depend on the value of the temperature, figure 8. For the values at the edges of the system design range there is a prevailing cross-correlation

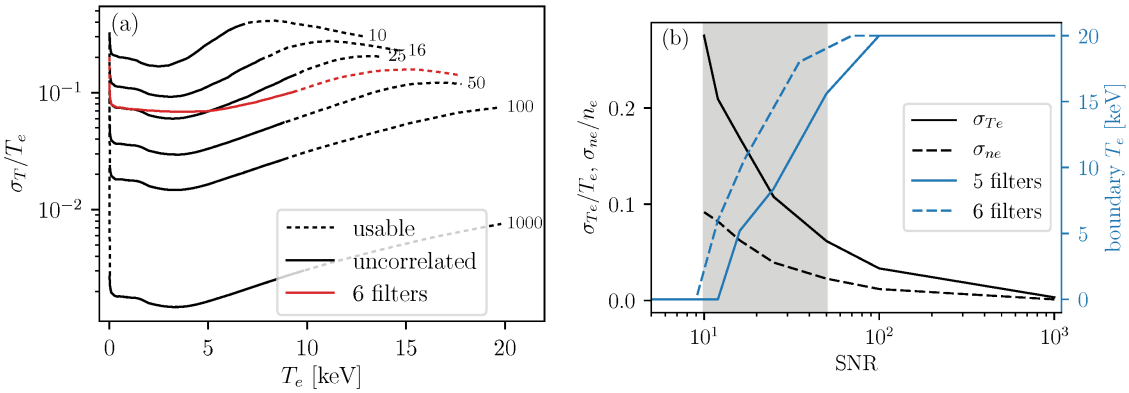

Figure 9. Scaling of errors with electron temperature and signal to noise ratio (SNR). (a) - dependence of the temperature uncertanty on the temperature for several SNR values. The black curves are for the standard W7-X polychromator with five spectral filters. The red curve is for a proposed 6-filter polychromator. (b) - dependence of the average temperature and density uncertanties on the SNR value. Also the boundary of the 12% uncertainty interval is shown for the 5 and 6 filter setups. The gray area indicates the SNR range obsrved in the first W7-X campaign.

between temperature and density. For example for temperature of 6 eV, the posterior has a banana like shape, and for temperature of 15.5 keV the distribution has a cigar shape. The upper boundary in the latter case is determined by the prior. Since in both cases the regular way of specifying the maximum and the uncertainties may turn problematic, they are considered here as being outside of the operational range. Nevertheless, such measurements can be useful if combined with other diagnostics. For temperatures away from the boundaries, temperatures of 15 eV and 9.5 keV in the figure, the distributions are more confined, but a significant T_e-n_e cross-correlation is still present and should be taken into account. In the middle of the temperature range, temperature of 110 eV in the figure, the distribution is very close to Gaussian without cross-correlation. In some cases, temperature of 6.5 keV in the figure, the distribution considerably deviates from Gaussian, but still has no cross-correlation. In such a case asymmetric uncertainties have to be specified.

Existence of some of the posterior shapes and the boundaries between them depend on the signal to noise ratio. In particular, the asymmetric distribution without cross-correlation illustrated by temperature of 6.5 keV is not pronounced for large SNR values. Instead a Gaussian distribution appears. Similarly, the cases with asymmetric cross-correlated distributions for 15 eV and 9.5 keV become very close to Gaussian distribution with cross-correlation, if SNR is high enough.

Results of the forward-inverse modelling are summarized in figure 9 in terms of uncertainties. The effective temperature uncertainty is plotted in figure 9a in dependence on the temperature for several SNR values. The uncertainty is defined here as width of the 95% confidence interval divided by four, it takes into account the cross-correlation but does not differentiate the asymmetry. The dashed lines cover the range where reliable measurements are possible, their boundaries correspond to the

banana and cigar shaped posterior from the discussion above. The solid lines show the range without cross-correlation between temperature and density. The SNR values are given for each line, the values being estimated from the maximal signal in all spectral channels. For the case of a very large SNR, the W7-X Thomson system is able to measure temperatures and densities without cross-correlation between about 10 eV and 10 keV. The value of uncertainty varies with temperature and has an optimum between about 1 keV and 5 keV. After the minimum, the uncertainty increases with the temperature. The roll-over visible for the low SNR cases is caused by the prior limit. For low SNR values, the measurement interval becomes narrower.

Scaling of the average temperature and density uncertainties with signal to noise ratio is shown in figure 9b. The values are averaged over the whole usable interval of temperatures. For example, to achieve a relative temperature error of 10% the SNR should be around 30, and for 5% error about 70. The SNR range covered in the first experimental campaign of W7-X is indicated in the figure for comparison. The density uncertainty is about two times lower than the temperature one, in agreement with $\sqrt{5}$. The temperature boundary at which the temperature uncertainty starts to exceed 12% is also presented in figure 9b. For high SNR values, reliable measurements are possible up to the end of the computation domain used here. Such performance is not achievable at all for SNR values less than about 10. The boundary of 12% is used here to carefully include the case with SNR of 16, but other values can be used as well.

It was realized in the first W7-X campaign that measurements of electron temperatures of 10 keV and above are important. The W7-X Thomson performance degrades for such temperatures, especially if SNR is poor. To improve the Thomson performance at such temperatures it is foreseen to add a sixth spectral channel to the central polychromators and to split the present channels 750–920 nm and 920–1000 nm into three: 730–850 nm, 850–940 nm and 940–1000 nm. This modification can be readily accomplished, because the polychromator chassis is designed for six channels. Improvement with the proposed 6 channel setup is illustrated in figure 9. The sixth channel indeed reduces the uncertainty for temperatures above about 5 keV and extends the measurement range. Further options for improving the system performance at high temperatures will be considered in future papers.

6. Thomson scattering measurements in OP1.1

The W7-X limiter campaign, OP1.1, lasted 10 weeks from December 2015 until March 2016. The plasma heating was provided by a 140 GHz electron cyclotron heating (ECRH) system with up to 4 MW of power. Because of a limited completion of the first wall, the total injected energy was limited to 4 MJ, corresponding to 1 s long discharges at full power and to up to 6 s long discharges at reduced power. Only feed forward density control was available and the achievable electron density was about $3 \cdot 10^{19}$ m^{-3} due to a limited wall conditioning. For such low densities, electron temperature of up to 7 keV strongly exceeds ion temperature of up to 2 keV, and the plasma is in the

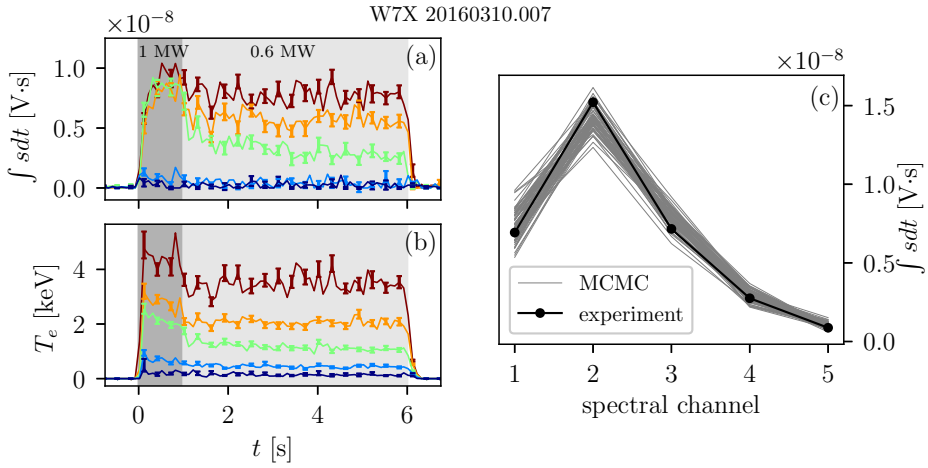

Figure 10. (a) - scattered pulse integral from the first spectral channel (750–920 nm) for scattering volumes 4 (center), 6, 8, 10 and 12 (edge). This example is for a 6 s long discharge with heating power of 1 MW before 1 s and 0.6 MW afterwards. The error bars show the 1σ range. (b) - electron temperature for the same scattering volumes. (c) - predictive posterior distribution for five spectral channels. This example is for scattering volume 4 at about 2.4 s. The black curve represents the measured values, and the gray curves are possible realizations sampled with Markov-Chain-Monte-Carlo procedure.

central electron root regime with positive radial electric field in the core [7, 8]. The overall plasma performance improved towards the end of the campaign as a result of better conditioned walls.

The Thomson scattering diagnostic operated reliably, with a very few exceptions, from the very first W7-X discharges. To improve the signal to noise ratio and the data reliability, a readjustment of the avalanche voltages was performed in the middle of the campaign, followed by a new calibration. A typical time resolved scattered light pulse together with the applied fitting can be found in figure 5b. The fitted pulse integrals are used to reconstruct both the electron temperature and the electron density with the help of the Bayessian model. Evolution of the fitted integral is illustrated in figure 10a for a 6 s long experiment having about a 4 s long plateau with ECRH heating of about 0.6 MW. The shown data are from the first spectral channel, 750–920 nm, of five scattering volumes from the center to the edge. The error bars represent the corresponding fit uncertainties. The reconstructed temperatures for the same discharge and for the same volumes are given in figure 10b. Both for the fit integral and for the calculated electron temperature and density, the estimated uncertainties agree with the standard deviations in flat top phases within about 30%.To achieve this parameters of the avalanche photodiodes were adjusted to match signal variation in Raman calibration. An independent calibration of the photodiodes is still to be developed.

Bayessian analysis can also be used to detect large scale systematic problems or inconsistency of the data. Figure 10c shows predictive posterior distribution of signals in five spectral channels for a central scattering volume together with the measured data. The

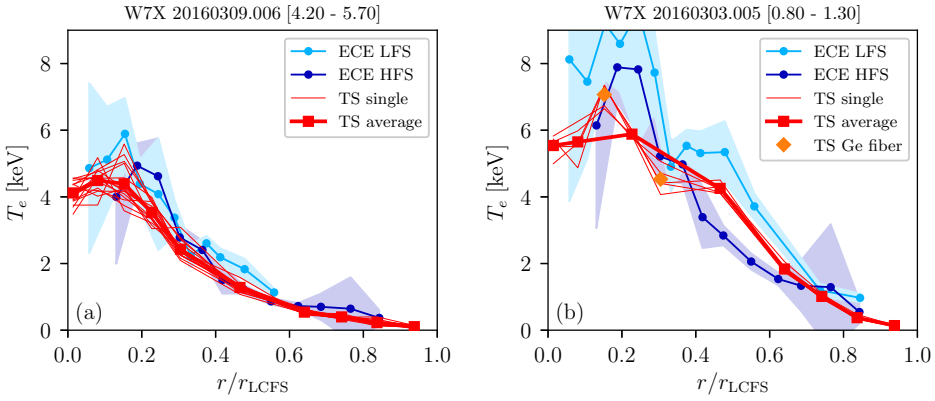

Figure 11. Comparison of electron temperature profiles measured with the Thomson scattering and electron cyclotron emission (ECE) diagnostics. The ECE diagnostic covers both sides of the profile. The colour filled areas show calibration uncertainties of the ECE calibration. (a) - 6 s discharge with ECRH power of about 0.6 MW, central electron density of about $1 \cdot 10^{19}$ m^{-3}, central and volume averaged β of about 0.25% and 0.13% correspondingly. (b) - discharge with ECRH power of about 3.8 MW, central electron density of about $2.1 \cdot 10^{19}$ m^{-3}, central and volume averaged β of about 0.8% and 0.5% correspondingly.

predictive posterior distribution is sampled with Markov-Chain-Monte-Carlo procedure around the most probable values for the given experimental data and their uncertainties. Since the measured data are typically well covered with predictive posterior and no clear outliers are observed, the validity of the model and of the calibration is supported. Smaller scale problems in the calibration, as those discussed below, are not easily indicated with this method and require a more elaborated treatment.

For discharges with the ECRH resonance on the axis, electron temperature is centrally peaked. Temperature profiles measured with the Thomson scattering diagnostic and with an electron cyclotron emission (ECE) diagnostic [33] are compared for plateau phases of two discharges in figure 11. The ECE data include both sides of the profile, the low field side (LFS) and the high field side (HFS), averaged over the full time intervals. The colour filled areas represent uncertainties of the ECE calibration, which is performed with a microwave source at liquid nitrogen and room temperatures. The Thomson scattering data are shown for every laser pulse with thin lines and as an average over the time intervals with symbols. Vacuum mapping to flux surface is assumed for both diagnostics and for both discharges.

The Thomson scattering measurements are in a good agreement with the ECE diagnostic in discharges with relatively low temperature and plasma pressure, figure 11a. In such cases also both sides of the ECE profile match. For higher temperatures and pressures the Thomson and ECE data are comparable, but some differences are observed, figure 11b. Two sides of the ECE measurements depart from each other, thus indicating a need for an equilibrium reconstruction. The Thomson measurements are about 20% lower in the center, and are between the LFS and HFS branches of the ECE

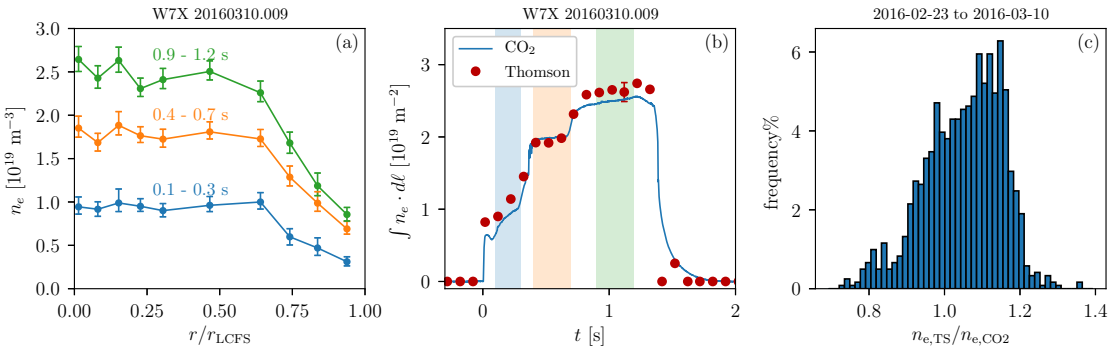

Figure 12. Profiles of electron density measured with Thomson scattering and comparison with a single channel interferometer. (a) - density profiles for three time intervals for a discharge, where the density was increased in three steps. The error bars indicate the 3σ measurement uncertainties and do not include calibration uncertainties. (b) - line integrated density measured with the CO_2 interferometer and calculated from the Thomson scattering data. (c) - statistics of the ratio of the line integrated density from the Thomson data and from the interferometer. In total about 1200 measurement points are included.

at the mid-radius. The Thomson scattering results for this case also show a remaining calibration issue for the channels with Ge-doped fibers: scattering volumes 3 and 5. Because the Ge-doped fibers have a larger numerical aperture, they are more sensitive to illumination conditions during spectral calibration. In addition, a smaller calibration imperfection can be suspected for volume 1 due to a possible shadowing by the in-vessel components. In order to improve the data consistency, both the calibration procedures will be further developed and a suitable equilibrium reconstruction will be used in future experiments.

Electron density profiles are typically flat in the center with a gradient reiong in the outer half for discharges with on-axis ECRH heating. Three density profiles measured with the Thomson scattering system are presented in figure 12a for a discharge where the density was raised in three steps. Each profile is averaged over 2 to 4 laser pulses in the indicated time intervals. The profiles are of similar shape, but have different amplitudes. In the central part of the profiles remaining systematic errors of the order of 5% are prominent. These errors are likely caused by the imperfect spectral calibration. The value of the error is consistent with the estimation from the Raman calibration in two spectral channels. It is worth noting that the shape of electron density profile can be affected by applying off-axis ECRH heating [8].

Electron densities measured with Thomson scattering can be validated against a single channel dispersion interferometer [34]. The laser path of the interferometer is designed to practically coincide with that of the Thomson scattering system. Therefore, if full profile is available from the Thomson system, such a comparison can be done without further assumptions by line integrating the Thomson data. In the first campaign only the outer half of the cross-section was covered, and as a consequence the values are

first mapped to the flux surfaces and afterwards are integrated along the interferometer chord. Thomson data integrated in this manner are compared in figure 12b with the interferometer data for the same discharge as used for profiles. Statistics of the ratio of the line integrated density from the two diagnostics is summarized in figure 12c for about 1200 Thomson laser pulses, which includes almost all measurements in the last three weeks of the campaign with exception of a very few discharges with a suspected laser misbehaviour. In general the Thomson scattering diagnostic overestimates the density by about 10%. It is further observed that the ratio changes slightly between experimental days. These changes can not be explained by the systematic uncertainty of the Raman calibration of about 5%, but are rather caused by changes in the laser adjustment. The adjustment can be indeed affected between experimental days because of an open access to the support structures. For this reason an automated laser position control is presently under development.
The Thomson scattering diagnostic operated reliably through out the first campaign and provided temperatures compatible with the ECE measurements and densities in a reasonable agreement with the single channel interferometer. Besides, the Thomson data are also used to estimate the kinetic plasma energy, where the electron contribution is the dominant one, and which is found to agree with the diamagnetic energy within about 25% [35]. One possible reasons for the discrepancy between the kinetic energy and the diamagnetic one is badly diagnosed impurity content. A further discussion of this comparison can be found in the reference. The experimental Thomson data also show remaining systematic errors, in particular in the spectral calibration of the channels with Ge-doped fibers and in the density calibration. These questions will be addressed in future experiments by improving the calibration procedures and by implementing a better laser control system.

7. Summary

Wendelstein 7-X is an optimized stellarator with superconducting coils [1,2], that started its operation in December 2015 and will perform the first divertor experiments and optimization validation in the second half of 2017. The W7-X incoherent Thomson scattering diagnostic for electron density and electron temperature is an essential tool for the physics program because of its good spatial resolution, reliability and coverage of the full density range between 10^{19}–$2 \cdot 10^{20}$ m^{-3}. In this paper the W7-X Thomson scattering diagnostic is described in details, including the setup, calibration procedures, data evaluation, example of the results from the first campaign and their comparison with other diagnostics, and plans for the system development.
The W7-X Thomson scattering diagnostic is a Nd:YAG system with up to five lasers, each with pulse energy from 0.7 to 2.4 J and repetition rate of 10 Hz, linearly polarized. The laser light is guided through the plasma roughly horizontally and close to the magnetic axis. Two sets of lenses observe the whole plasma cross-section of about 1.6 m

from the top with optical demagnification between 7 and 11 and solid angle of the order of 8 msr. The system geometry allows a direct measurement of Shafranov shift of magnetic flux surfaces in addition to the usual profile information. The laser mirrors and the optics sets are mechanically decoupled from the machine, thus ensuring optical stability.

The scattered light is transferred with fiber bundles to filter based polychromators for the spectral analysis. To save hardware costs, some bundles are combined to a single polychromator, with one of the bundles having a delay loop of 20 m. Such an approach proved to be reliable and to cause a tolerable increase in the noise level. Presently, five spectral channels are used to cover the electron temperatures from about 10 eV up to about 10 keV: 750–920 nm, 920–1000 nm, 1000–1035 nm, 1035–1051 nm and 1051–1061 nm. The optical signals are registered with temperature stabilized avalanche photodiodes. The photodiode outputs are AC filtered, amplified and digitized with sampling rate of 1 GS/s and 14 bit vertical resolution. The acquisition system records time resolved laser pulses, which helps to recognize reflections and improves the signal to noise ratio.

The relative spectral calibration of the system is carried out with the help of a pulsed supercontinuum light source and of a scanning monochromator, where the source delivers a flat spectrum and the monochromator selects a wavelength for each measurement. The wavelengths are referenced by using 808 nm and 1064 nm lines present in the spectrum, the spectral resolution is estimated to be about 0.4 nm. The monochromatized light is delivered to a diffuse screen in front of the collection optics, and in such a way the calibration procedure includes the front optics, the fiber bundles, the polychromators and the electronics. The angular distribution of the intensity in the calibration setup is not fully equivalent to that during plasma measurements. These effects are possible reasons for the remaining small systematic errors in the electron temperature measurements.

The absolute calibration of the system is performed by observing anti-Stokes rotational Raman scattering in nitrogen in two spectral channels. The dependence of the Raman signals in both channels on the nitrogen density is close to linear, with statistical uncertainty of the slope and consequently of the calibration factors of about 1%. However, the factors calculated using the two spectral channels do show a difference for some volumes. This is likely caused by imperfections of the spectral calibration. A wavelength shift of 0.25 nm brings both spectral channels to agreement, resulting in an error estimation of about 4%. In addition, the absolute factors have a uniform systematic uncertainty of 5% due to the available molecular data.

The electron temperatures and densities are recovered by Bayesian modelling with Minerva framework [20], which is a versatile Java framework with implementations for finding the maximum of the posterior, sampling of the posterior with Markov-Chain-Monte-Carlo (MCMC) method, etc. The Bayesian approach provides asymmetries of the uncertainties and the cross-correlation between density and temperature, and allows to include uncertainties of the calibration parameters, to introduce a profile description,

and to combine multiple diagnostics. In this work, a Bayesian model for Thomson scattering is developed, is used to analyze the system performance, and is applied to experiments.

To test the Bayessian model and to verify the system performance simulations with synthetic data are used. Different types of the posterior distribution are found for different values of the signal to noise ratio and different temperature ranges. At the edges of the system temperature range, there is a prevailing cross-correlation between temperature and density: a banana like shape for low temperatures, and an open cigar shape at high temperatures. Close to Gaussian posterior distributions with or without the cross-correlation are usually observed in the middle of the design range. In some cases considerable deviations from Gaussian are observed, so that asymmetric uncertainties have to be specified. It is confirmed that with the present choice of filters and for large SNR the W7-X Thomson system is suitable for measurements without the cross-correlation for temperatures between 10 eV and 10 keV. The measurement interval becomes narrower for lower SNR values. To achieve a relative temperature error of 10% the SNR should be around 30, and for 5% error it should be about 70.

In the first campaign, OP1.1, the Thomson scattering diagnostic operated reliably from the very first W7-X discharges. In this phase, the system included one Nd:YAG laser and 10 scattering volumes on the outboard half of the profile. For discharges with the ECRH resonance on the axis, electron temperature is found to be centrally peaked, whereas the electron density is flat in the center with a gradient region in the outer half. Temperature profiles measured with the Thomson scattering diagnostic are in a good agreement with an independently calibrated electron cyclotron emission (ECE) diagnostic in discharges with relatively low temperature and plasma pressure. Some differences are observed for higher temperatures and pressures: the low field side and the high field side of the ECE measurements depart from each other; the Thomson data are up to 20% lower in the center, and are between the two ECE branches at the mid-radius. The Thomson scattering results for the latter case also show a remaining calibration issue for the channels with Ge-doped fibers, which are more sensitive to illumination conditions because of their larger numerical aperture. In order to improve the data consistency, both the calibration procedures have to be further refined and a suitable equilibrium reconstruction should be used.

Electron density profiles measured with the Thomson scattering system indicate systematic errors between channels of the order of 5%. These errors are likely due to imperfections of the spectral calibration. The absolute values of the density are in a reasonabke agreement with a single channel dispersion interferometer. The Thomson scattering diagnostic tends to overestimate the line integrated density by about 10%. It is observed that this discrepancy changes slightly between experimental days, as can be caused by changes in the laser adjustment between experimental days because of an open access to the support structures. For this reason an automated laser position control is presently under development.

The W7-X Thomson scattering system will be further extended for future experiments.

Three lasers will be taken into operation, which will allow either a higher repetition rate of 30 Hz, a higher pulse energy of up to 6 J at 10 Hz, or a pulse train operation with 12 pulses each 100 μs with repetition rate of 5 Hz. The spatial resolution of the system will be improved and both sides of the profile will be covered. The outboard side will be extended to 16 scattering volumes by filling available gaps in the holder. The inboard part of the profile will be equipped with fibers for 79 volumes giving spatial resolution of 6 mm in effective radius in the gradient region. Here fiber bundles of different lengths without ferrule will be densely packed side by side. Polychromators for the inboard side will be added in several steps. To improve the Thomson performance at temperatures above 10 keV it is foreseen to add a sixth spectral channel and to split filters 750–920 nm and 920–1000 nm into: 730–850 nm, 850–940 nm and 940–1000 nm. For temperatures above 15 keV, two wavelength measurements with the second laser at 1.3 μm are planned. To improve the spectral calibration, a new scheme employing Rayleigh scattering from a tunable wavelength laser is under devolpment. This approach will remove the uncertainty due to illumination conditions and also will include the vacuum window and the deposited layers into the calibration.

Acknowledgment.

Authors would like to thank Dr. R. Yasuhara for useful discussions and Dr. O. Ford for help with Minerva framework.
This work has been carried out within the framework of the EUROfusion Consortium and has received funding from the Euratom research and training programme 2014-2018 under grant agreement No 633053. The views and opinions expressed herein do not necessarily reflect those of the European Commission.

References

[1] Grieger G, Beidler C, Harmeyer E, Junker J, Kißlinger J, Lotz W, Merkel P, Montvai A, Nührenberg J, Rau F, Schlüter A, Wobig H and Zille R 1989 Physics studies for helical-axis advanced stellarators Plasma Physics and Controlled Nuclear Fusion Research, Proceedings of the 12th International Conference, Nice, 1988 vol 2 (IAEA, Vienna) pp 369 – 387

[2] Beidler C, Grieger G, Herrnegger F, Harmeyer E, Kisslinger J, Lotz W, Maassberg H, Merkel P, Nuhrenberg J, Rau F, Sapper J, Sardei F, Scardovelli R, Schluter A and Wobig H 1990 Fusion Technology **17** 148–168

[3] Wolf R C, Beidler C D, Dinklage A, Helander P, Laqua H P, Schauer F, Pedersen T S and Warmer F 2016 IEEE Transactions on Plasma Science **44** 1466–1471 ISSN 0093-3813

[4] Grieger G, Lotz W, Merkel P, Nührenberg J, Sapper J, Strumberger E, Wobig H, Burhenn R, Erckmann V, Gasparino U, Giannone L, Hartfuss H J, Jaenicke R, Kühner G, Ringler H, Weller A, Wagner F, W7-X Team and W7-AS Team (W7-X Team and W7-AS Team) 1992 Physics of Fluids B: Plasma Physics **4** 2081–2091 URL `http://link.aip.org/link/?PFB/4/2081/1`

[5] Nührenberg J 2010 Plasma Physics and Controlled Fusion **52** 124003 URL `http://stacks.iop.org/0741-3335/52/i=12/a=124003`

[6] Pedersen T S, Andreeva T, Bosch H S, Bozhenkov S, Effenberg F, Endler M, Feng Y, Gates D, Geiger J, Hartmann D, Hlbe H, Jakubowski M, Knig R, Laqua H, Lazerson S, Otte M, Preynas

M, Schmitz O, Stange T, Turkin Y and the W7-X Team 2015 Nuclear Fusion **55** 126001 URL http://stacks.iop.org/0029-5515/55/i=12/a=126001

[7] Klinger T, Alonso A, Bozhenkov S, Burhenn R, Dinklage A, Fuchert G, Geiger J, Grulke O, Langenberg A, Hirsch M, Kocsis G, Knauer J, Krmer-Flecken A, Laqua H, Lazerson S, Landreman M, Maaberg H, Marsen S, Otte M, Pablant N, Pasch E, Rahbarnia K, Stange T, Szepesi T, Thomsen H, Traverso P, Velasco J L, Wauters T, Weir G, Windisch T and Team T W X 2017 Plasma Physics and Controlled Fusion **59** 014018 URL http://stacks.iop.org/0741-3335/59/i=1/a=014018

[8] Wolf R C and et al 2017 submitted to Nuclear Fusion

[9] Kißlinger J, Beidler C D, Harmeyer E, Rau F, Renner H and Wobig H 1994 Island divertor for the stellarator Wendelstein 7-X Controlled Fusion and Plasma Physisc, Proceedings of 21st European Conference, Montpellier, 1994 vol 18B, part 1 (European Physical Society, Geneva) pp 368 – 371

[10] Greuner H, Bitter W, Kerl F, Kißlinger J and Renner H 1995 Structure of divertor for the optimized stellarator W7-X Fusion Technology, Proceedings of 18th Symposium Karlsruhe, 1994 vol 1 (Elsevier, Amsterdam and New-York) pp 323 – 326

[11] Renner H, Boscary J, Erckmann V, Greuner H, Grote H, Sapper J, Speth E, Wesner F and Wanner M 2000 Nuclear Fusion **40** 1083 – 1093

[12] Fuchert G, Bozhenkov S, Beurskens M, Dinklage A, Feng Y, Geiger J, Helander P, Hirsch M, Hoefel U, Jakubowski M, Knauer J, Langenberg A, Laqua H, Maassberg H, Moseev D, Niemann H, Zhang D, Pasch E, Rahbarnia K, Stange T, Mora H T, Turkin J, Pablant N, Wurden G and Wolf R 2016 Global energy confinement in the first operational phase of Wendelstein 7-X, PO4.00001 58th Annual Meeting of the APS Division of Plasma Physics; October 31November 4 2016; San Jose, California

[13] Hirsch M and et al 2017 submitted to Nuclear Fusion

[14] Hutchinson I 2005 Principles of Plasma Diagnostics (Cambridge University Press) ISBN 9780521675741 URL https://books.google.de/books?id=pUUZKLR00RIC

[15] Pasqualotto R, Nielsen P, Gowers C, Beurskens M, Kempenaars M, Carlstrom T, Johnson D and Contributors J E 2004 Review of Scientific Instruments **75** 3891–3893 (*Preprint* http://dx.doi.org/10.1063/1.1787922) URL http://dx.doi.org/10.1063/1.1787922

[16] Kurzan B and Murmann H D 2011 Review of Scientific Instruments **82** 103501 (*Preprint* http://dx.doi.org/10.1063/1.3643771) URL http://dx.doi.org/10.1063/1.3643771

[17] Yamada I, Narihara K, Funaba H, Yasuhara R, Kohmoto T, Hayashi H, Hatae T, Tojo H, Sakuma T, Yoshida H, Fujita H and Nakatsuka M 2012 Journal of Instrumentation **7** C05007 URL http://stacks.iop.org/1748-0221/7/i=05/a=C05007

[18] Naito O, Yoshida H and Matoba T 1993 Physics of Fluids B **5** 4256–4258

[19] Naito O, Yoshida H and Matoba T 1994 Physics of Plasmas **1** 806

[20] Svensson J, Dinklage A, Geiger J, Werner A and Fischer R 2004 Review of Scientific Instruments **75** 4219–4221 URL http://link.aip.org/link/?RSI/75/4219/1

[21] Fischer R, Wendland C, Dinklage A, Gori S, Dose V and the W7-AS team 2002 Plasma Physics and Controlled Fusion **44** 1501 URL http://stacks.iop.org/0741-3335/44/i=8/a=306

[22] Fischer R, Dinklage A and Pasch E 2003 Plasma Physics and Controlled Fusion **45** 1095 URL http://stacks.iop.org/0741-3335/45/i=7/a=304

[23] Kwak S, Svensson J, Bozhenkov S, Flanagan J, Kempenaars M and Ghim Y C 2016 Bayesian modelling of JET high resolution Thomson scattering system using the Minerva framework, TO7.00014 58th Annual Meeting of the APS Division of Plasma Physics, October 31–November 4 2016, San Jose, California vol 61

[24] Pasch E, Beurskens M N A, Bozhenkov S A, Fuchert G, Knauer J and Wolf R C 2016 Review of Scientific Instruments **87** 11E729 (*Preprint* http://aip.scitation.org/doi/pdf/10.1063/1.4962248) URL http://aip.scitation.org/doi/abs/10.1063/1.4962248

[25] Cantarini J, Knauer J P and Pasch E 2008 AIP Conference Proceedings **993** 191–194 (*Preprint* http://aip.scitation.org/doi/pdf/10.1063/1.2909106) URL http://aip.scitation.org/doi/abs/10.1063/1.2909106

[26] Howard J, James B W and Smith W I B 1979 Journal of Physics D: Applied Physics **12** 1435 URL http://stacks.iop.org/0022-3727/12/i=9/a=005

[27] LeBlanc B P 2008 Review of Scientific Instruments **79** 10E737 URL http://scitation.aip.org/content/aip/journal/rsi/79/10/10.1063/1.2956747

[28] Yamada I, Narihara K, Hayashi H and Group L E 2003 Review of Scientific Instruments **74** 1675–1678 URL http://scitation.aip.org/content/aip/journal/rsi/74/3/10.1063/1.1538362

[29] Penney M, Peters R S and Lapp M 1974 Journal of Optical Society of America **64** 712–716

[30] Schrötter H and HW K 1979 Raman scattering cross sections in gases and liquids in Raman spectroscopy of gases and liquids Topics in current physics (Springer-Verlag)

[31] Bendtsen J 1974 Journal of Raman Spectroscopy **2** 133–145 ISSN 1097-4555 URL http://dx.doi.org/10.1002/jrs.1250020204

[32] Sivia D S and Skilling J 2006 Data Analysis: A Bayesian Tutorial Oxford science publications (Oxford University Press) ISBN 9780198568322 URL https://books.google.de/books?id=zN-yliq6eZ4C

[33] Hirsch M, andT Estrada R B, Hartfuss H J, Kasparek W, Krmer-Flecken A, Kppen M, Kornejew P, Lechte C, Neuner U, Plaum B, Standley B, Stange T, Trimino-Mora H, Windisch T, Wagner D and Wolf R 2014 Microwave and interferometer diagnostics for Wendelstein 7-X 41st EPS Conf. on Plasma Physics, Berlin, Germany (2014), P1.069; URL http://ocs.ciemat.es/EPS2014PAP/pdf/P1.069.pdf

[34] Knauer J, Kornejew P, Trimino Mora H, Hirsch M, Werner A and Wolf R 2016 A new dispersion interferometer for the stellarator Wendelstein 7-X 43rd EPS Conf. on Plasma Physics, Leuven, Belgium (2016), P4.017; URL http://ocs.ciemat.es/EPS2016PAP/pdf/P4.017.pdf

[35] Fuchert G to be published